NANO LETTERS

Letter

pubs.acs.org/NanoLett

Porous Graphene Nanoarchitectures: An Efficient Catalyst for Low Charge-Overpotential, Long Life, and High Capacity Lithium–Oxygen Batteries

Bing Sun,[†] Xiaodan Huang,[†] Shuangqiang Chen,[†] Paul Munroe,[‡] and Guoxiu Wang*[,†]

[†]Centre for Clean Energy Technology, School of Chemistry and Forensic Science, University of Technology Sydney, 15 Broadway, Sydney, New South Wales 2007, Australia

[‡]Electron Microscope Unit, The University of New South Wales, Sydney, New South Wales 2052, Australia

Supporting Information

ABSTRACT: The electrochemical performance of lithium–oxygen ($Li–O_2$) batteries awaits dramatic improvement in the design of porous cathode electrodes with sufficient spaces to accommodate the discharge products and discovery of effective cathode catalysts to promote both oxygen reduction reactions and oxygen evolution reactions. Herein, we report the synthesis of porous graphene with different pore size architectures as cathode catalysts for $Li–O_2$ batteries. Porous graphene materials exhibited significantly higher discharge capacities than that of nonporous graphene. Furthermore, porous graphene with pore diameter around 250 nm showed the highest discharge capacity among the porous graphene with the small pores (about 60 nm) and large pores (about 400 nm). Moreover, we discovered that addition of ruthenium (Ru) nanocrystals to porous graphene promotes the oxygen evolution reaction. The Ru nanocrystal-decorated porous graphene exhibited an excellent catalytic activity as cathodes in $Li–O_2$ batteries with a high reversible capacity of 17 700 mA h g^{-1}, a low charge/discharge overpotential (about 0.355 V), and a long cycle life up to 200 cycles (under the curtaining capacity of 1000 mAh g^{-1}). The novel porous graphene architecture inspires the development of high-performance $Li–O_2$ batteries.

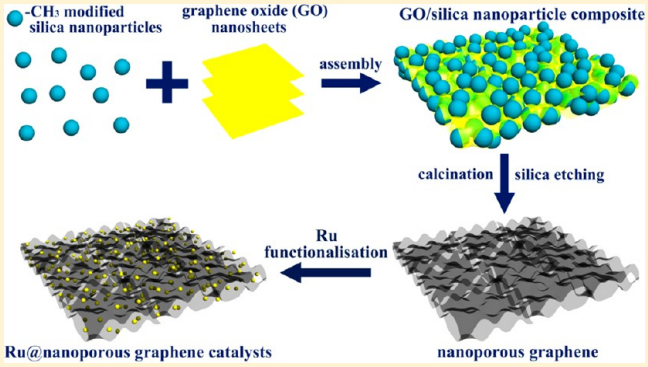

KEYWORDS: *Lithium–oxygen battery, porous graphene, cathode catalyst, ruthenium nanocrystals*

Rechargeable $Li–O_2$ batteries are considered to be one of the most promising systems for meeting today's stringent requirements as the power source for electric vehicles.[1] The theoretical specific energy of the $Li–O_2$ battery is 3505 Wh kg^{-1}, which is almost ten times higher than that of Li-ion batteries (387 Wh kg^{-1}).[2,3] However, the development of $Li–O_2$ batteries is still constrained by several serious challenges, including poor cycling stability, low charge/discharge electrical efficiency, and low rate capability.[4−6] A typical rechargeable $Li–O_2$ battery consists of a porous oxygen diffusion cathode, a lithium metal anode and a Li^+ conducting electrolyte. During the battery operation, oxygen is drawn from the air atmosphere and reduced by lithium ions from the electrolyte to form Li_2O_2 (oxygen reduction reactions, ORRs) in the discharge process. During the charge process, the discharge products electrochemically decompose to lithium ions and oxygen (oxygen evolution reactions, OERs).[7−9] Because the discharge product cannot be dissolved in organic electrolyte, the irregular deposition of Li_2O_2 in the cathode not only blocks the oxygen diffusion path, but also causes severe volume expansion of the electrode, leading to degradation of the electrode. Tuning the porous structure of the cathode materials is essential to improve the performance of $Li–O_2$ batteries. Previous studies have revealed that carbon materials with large pore volume and uniform pore-size distribution can increase the specific capacity of $Li–O_2$ batteries.[10−12] Furthermore, porous carbon cathodes such as hierarchically porous honeycomb-like carbon and ordered hierarchical mesoporous/macroporous carbon demonstrated improved discharge capacities.[13−17] Therefore, optimizing the pore structure of the carbon materials is an efficient way to improve the electrochemical performance of $Li–O_2$ batteries.

The other major challenge for the development of rechargeable $Li–O_2$ batteries is to reduce the large charge/discharge voltage gap to increase the energy efficiency. Although the commonly used carbon materials are good catalysts for the ORRs, they are not sufficient for the OERs.[18,19] Tremendous efforts have been devoted to explore various cathode catalysts to address this challenge.[20] Many catalysts have been investigated to promote the ORRs and OERs, such as nitrogen-doped carbon,[21−23] metal oxides,[24−30] metal

Received: January 31, 2014
Revised: May 14, 2014
Published: May 22, 2014

Scheme 1. Schematic Illustration for Synthesis of Porous Graphene and Ru-Functionalized Nanoporous Graphene Architectures

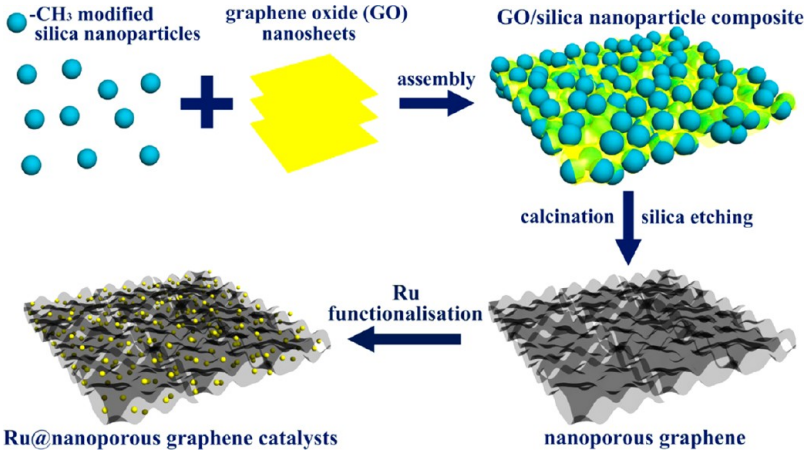

nitrides,[31] and precious metals.[32−34] Recently, Ru and RuO_2 have been reported as active catalysts toward the OERs. Li−O_2 cells with Ru-based catalysts showed a high reversible capacity, low charge overpotential and good cycling stability.[35−39]

In this paper, we developed an efficient cathode catalyst, ruthenium nanocrystal-functionalized porous graphene architectures. The tailored, highly porous graphene with uniform pores around 250 nm provides sufficient voids to accommodate Li_2O_2 and facilitate oxygen diffusion through the electrode. It has been proved that the porous structure is an important factor to influence the overall electrochemical performances of Li−O_2 batteries. Ru nanocrystals can efficiently reduce the charge overpotential and increase the cycling stability.

Results and Discussion. The graphene nanoarchitectures with highly porous structure were synthesized by a hard template method.[40] Scheme 1 shows the schematic illustration of the synthesis process of porous graphene. The silica nanospheres were first prepared by the well-known Stöber method. They were then functionalized with surface methyl groups and mixed with the graphene oxide (GO) nanosheets suspension to form GO/silica composites. The as-prepared composites were then calcinated in the inert atmosphere to reduce GO into graphene. The final products were obtained by removing the silica templates. Four samples were prepared with different pore structures. Nonporous graphene was synthesized by direct calcination of the GO in the inert atmosphere (Figure S1, Supporting Information) and is denoted as PGE-0. The porous graphene with pore size of about 60 nm was synthesized using silica nanosphere templates (Figure S2, Supporting Information) and is denoted as PGE-1. SEM and TEM images clearly show a nanoporous structure throughout the entire sample (Figure 1a,b). The N_2 adsorption−desorption plots of PGE-1 sample (Figure S3a, Supporting Information) show a type IV isotherm with a steep increase of nitrogen absorption at a high relative pressure (P/P_0 = 0.80−0.99), indicating that the main pore volume is contributed by large size pores. PGE-1 has a surface area of 242 m^2 g^{-1} and a large pore volume of 1.9 cm^3 g^{-1}. The pore sizes are mainly distributed at 62.4 nm (Figure S3b, Supporting Information), which is close to the particle diameter of the silica nanosphere hard templates. The porous graphene with pore size about 250 nm was also synthesized by using the silica template shown in Figure S4 (Supporting Information) and denoted as PGE-2. These pores of 250 nm are clearly shown in the SEM image in Figure 1c. TEM image also presents the highly porous architecture with spherical pores (Figure 1d). The N_2 adsorption−desorption analysis results reveal that the PGE-2 has a high surface area of 374 m^2 g^{-1} and a large pore volume of 1.5 cm^3 g^{-1} (Figure S5, Supporting Information). In order to further demonstrate that the hard template method is effective to synthesize porous graphene with controlled pore size, we further synthesized porous graphene with nanorod-shaped pores. The porous graphene with pore size about 200 nm wide and 400 nm long was synthesized by using the nanorod-shaped silica template shown in Figure S6 (Supporting Information) and denoted as PGE-3. These nanorod-shaped pores are clearly shown in the SEM image in Figure S7a (Supporting Information). TEM images at different magnification also present the highly porous architecture with nanorod-shaped pores (Figure S7b−d, Supporting Information). The N_2 adsorption−desorption analysis results reveal that the PGE-3 has a high surface area of 358 m^2 g^{-1} and a pore volume of 1.15 cm^3 g^{-1} (Figure S8, Supporting Information).

The Ru nanocrystal-functionalized porous graphene (Ru@PGE-2) was synthesized by an impregnation method. PGE-2 was mixed with a $RuCl_3$ solution overnight and separated by filtration. The final product was obtained by heat treatment in the reducing atmosphere. The ruthenium content in the Ru@PGE-2 nanocomposite was determined to be 20.34 wt % calculated using the TGA measurement (Figure S9, Supporting Information). Figure S10 (Supporting Information) shows the X-ray diffraction (XRD) patterns of PGE-2 and Ru@PGE-2 composite, in which two main diffraction peaks can be indexed to graphene (002) and Ru (101) in the XRD pattern of the Ru@PGE-2 composite. The SEM image (Figure S11, Supporting Information) shows a similar porous structure as the PGE-2 sample, indicating that the pore structure has been preserved following the Ru nanocrystal functionalization process. The TEM image shows that Ru nanocrystals are homogeneously distributed on the porous graphene matrix (Figure 1e). High-resolution TEM imaging further clearly demonstrates that Ru nanocrystals were uniformly anchored on the surface of graphene nanosheets (Figure 1f). The selected area electron diffraction (SAED) pattern (the inset in Figure 1f) can be indexed to the (101) lattice of Ru nanocrystals. The N_2 adsorption−desorption analysis identified that the Ru@PGE-2 has a surface area of 254 m^2 g^{-1} with a pore volume of 0.87 cm^3 g^{-1} (Figure S12, Supporting Information).

dx.doi.org/10.1021/nl500397y | Nano Lett. 2014, 14, 3145−3152

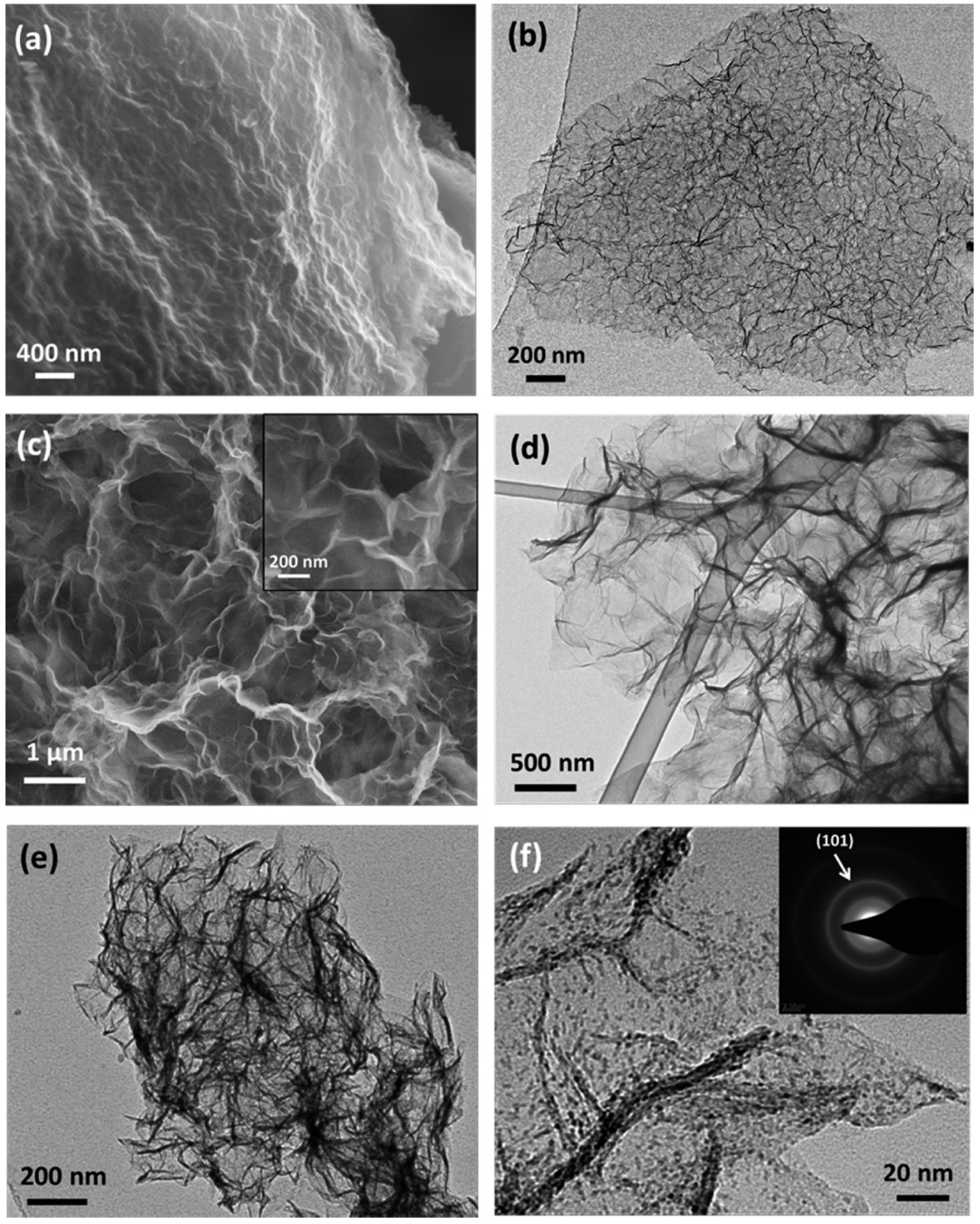

Figure 1. (a) SEM image and (b) TEM image of PGE-1. (c) SEM image and (d) TEM image of PGE-2. (e,f) TEM images of Ru@PGE-2 and the SAED pattern (inset).

The electrochemical performances of porous graphene as cathode catalysts were examined in Li−O_2 cells and compared with nonporous graphene in DMSO-based electrolyte.[9,41,42] The galvanostatic charge/discharge measurements were carried out to evaluate the electrochemical performances in the voltage range of 2.0−4.6 V at the current density of 200 mA g^{-1}. The typical charge/discharge voltage profiles are shown in Figure 2a. The discharge capacity of the PGE-2 electrode is 29 375 mA h g^{-1}, which is higher than the PGE-1 and PGE-3 electrode (20 310 and 22 458 mA h g^{-1}, respectively). All porous graphene electrodes show much higher discharge capacities than the nonporous graphene electrode. The discharge capacity of the PGE-0 electrode is only 8306 mA h g^{-1}. The rate performance of the porous graphene was further investigated at higher charge/discharge current densities of 500, 1000, and 2000 mA g^{-1}, respectively (as shown in Figure 2b,c and Figure S13, Supporting Information). The PGE-1 electrode shows good high C-rate performances with discharge capacities of 15 996 mA h g^{-1} at 500 mA g^{-1}, 10 937 mA h g^{-1} at 1000 mA g^{-1}, and 5645 mA h g^{-1} at 2000 mA g^{-1}. The PGE-2 electrode delivered improved discharge capacities of 22 173 mA h g^{-1} at 500 mA g^{-1}, 11 718 mA h g^{-1} at 1000 mA g^{-1} and 6187 mA h g^{-1} at 2000 mA g^{-1}. Meanwhile, the PGE-3 electrode also showed good high C-rate performances with discharge capacities of 13 849 mA h g^{-1} at 500 mA g^{-1}, 10 065 mA h g^{-1} at 1000 mA g^{-1}, and 6212 mA h g^{-1} at 2000 mA g^{-1}. It should be noted that all

dx.doi.org/10.1021/nl500397y | *Nano Lett.* 2014, 14, 3145−3152

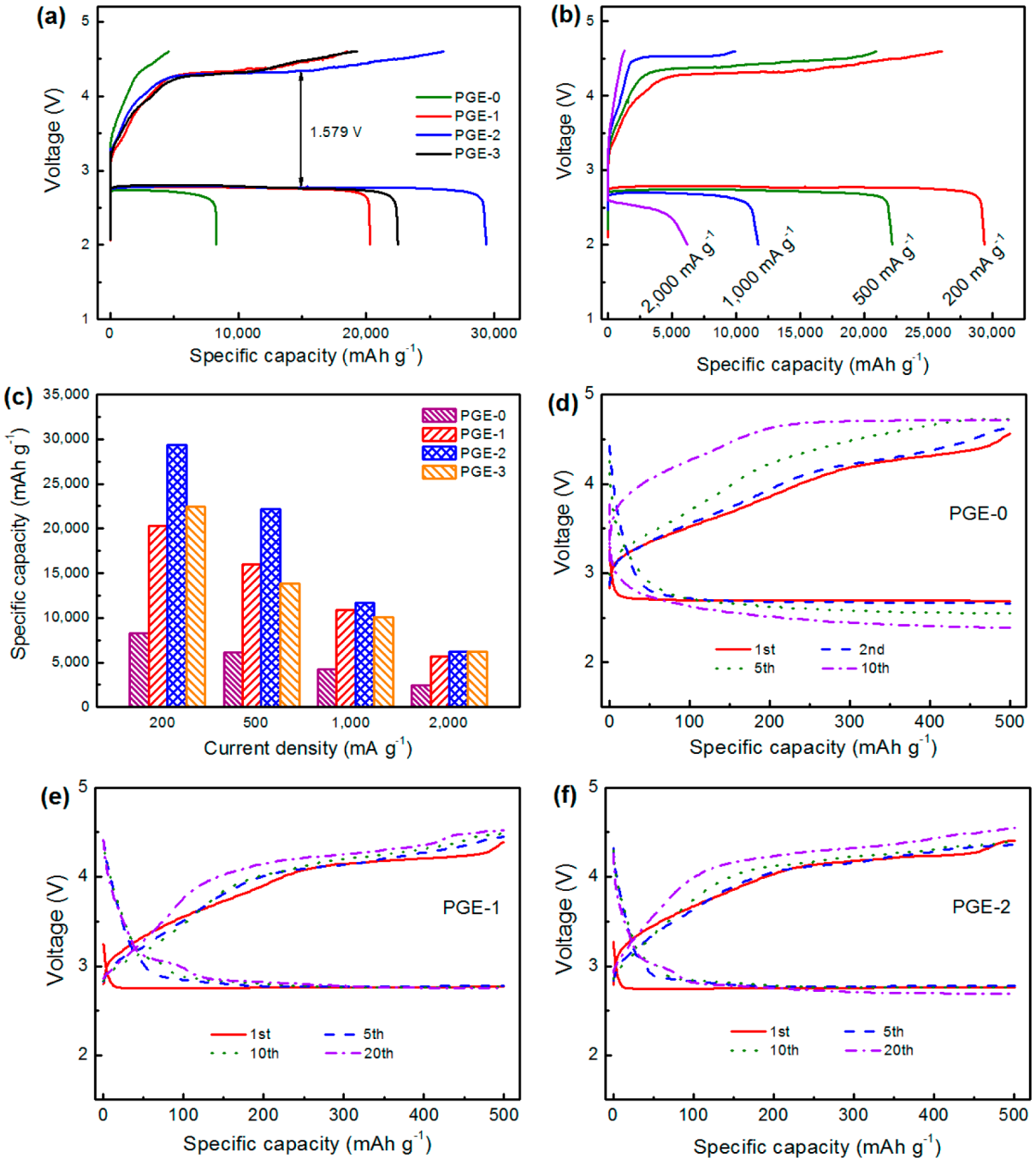

Figure 2. (a) Charge/discharge profiles of Li−O_2 batteries with PGE-0, PGE-1, PGE-2, and PGE-3 as cathode catalysts at the current density of 200 mA g^{-1}. (b) Charge/discharge profiles of Li−O_2 batteries with PGE-2 cathode catalysts at different current densities. (c) The discharge specific capacities of Li−O_2 batteries with PGE-0, PGE-1, PGE-2, and PGE-3 as cathode catalysts at different current densities. Cycling performance of Li−O_2 batteries based on (d) PGE-0, (e) PGE-1, and (f) PGE-2 cathode catalysts (at 200 mA g^{-1} by curtailing capacity to 500 mA h g^{-1}).

the porous graphene electrodes exhibited much better C-rate performance than nonporous graphene electrode, indicating the porous architecture can provide sufficient space to accommodate the discharge products and facilitate the oxygen diffusion through the electrode. The cycling performances of porous graphene catalysts were examined in the voltage range of 2.0−4.6 V at 500 mA g^{-1} (as shown in Figure S14, Supporting Information). All three porous graphene electrodes exhibited better capacity retention than the nonporous graphene in the first three cycles. The capacity fading during cycling could be caused by the volume change of the electrode due to the accumulation of large amount of discharge products during deep discharge, which may induce the collapse of the porous structure. We further examined the cycling performances of porous graphene catalysts by curtailing the capacity to 500 mA h g^{-1} (as shown in Figure 2d−f and Figure S15, Supporting Information).[43] The charge/discharge overpotential of the PGE-0 electrode significantly increased at the tenth cycle. However, porous graphene electrodes showed good cycling stability in the first 20 cycles, demonstrating that the porous structure is an important factor for maintaining the cycling stability of Li−O_2 cells. The PGE-2 sample exhibited the best

dx.doi.org/10.1021/nl500397y | Nano Lett. 2014, 14, 3145−3152

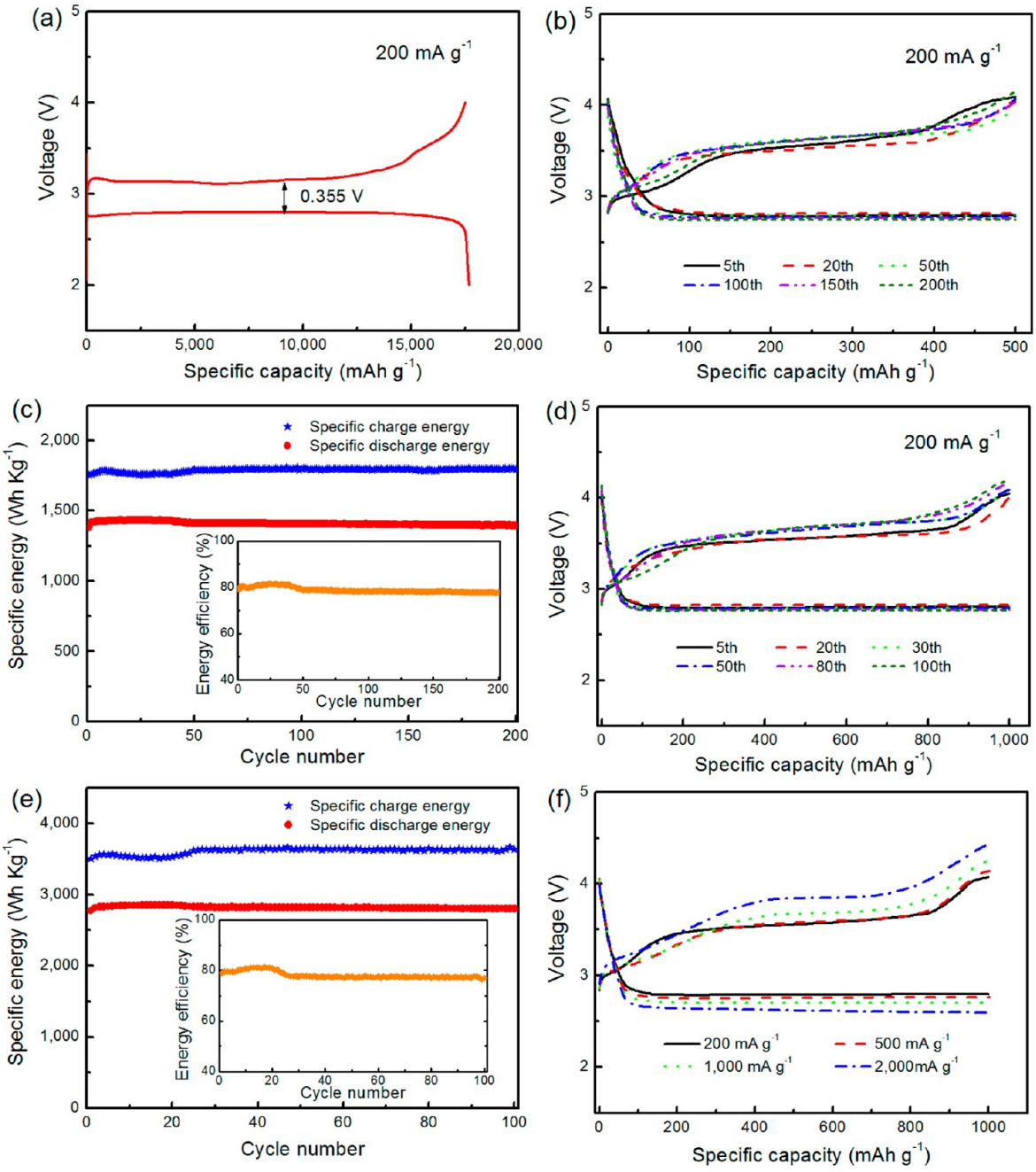

Figure 3. (a) First cycle charge/discharge profiles of Li−O_2 batteries with Ru@PGE-2 as cathode catalysts at 200 mA g^{-1} in the voltage range of 2.0−4.4 V. (b) Charge/discharge profiles at different cycles and (c) specific energy versus cycle number of Li−O_2 battery with Ru@PGE-2 catalysts at 200 mA g^{-1} by curtailing the capacity to 500 mA h g^{-1} in the voltage range of 2.0−4.4 V. (d) Charge/discharge profiles at different cycles and (e) specific energy versus cycle number of Li−O_2 battery with Ru@PGE-2 catalysts at 200 mA g^{-1} by curtailing the capacity to 1000 mA h g^{-1} in the voltage range of 2.0−4.4 V. (f) Charge/discharge profiles of Li−O_2 battery with Ru@PGE-2 catalysts at different current densities. The inset panels in (c) and (e) are the corresponding energy efficiency versus cycle number.

electrochemical performance among all porous graphene samples.

Ru nanocrystals have been demonstrated to be an effective cathode catalyst for ORRs and OERs.[33,35,36] We decorated porous graphene with Ru nanocrystals to increase the charge/discharge energy efficiency and cycling performance of Li−O_2 batteries. The galvanostatic charge/discharge measurements were carried out to evaluate the electrochemical performances of Ru@PGE-2 catalysts at room temperature. The typical charge/discharge voltage profiles are shown in Figure 3a. The discharge capacity of the Ru@PGE-2 catalysts is 17 710 mA h g^{-1}, which is lower than the bare PGE-2 graphene electrode (29 375 mA h g^{-1}). The decrease of capacity might be ascribed to be the occupation of Ru nanocrystals in PGE-2 pores. The discharge plateau of Ru@PGE-2 electrode is 2.79 V, which is similar to the PGE-2 electrode (2.78 V). For the charge process, significant differences were observed between Ru@PGE-2 electrode and PGE-2 electrode. The Ru@PGE-2 electrode shows a charge voltage plateau at 3.15 V, which is much lower than that of the PGE-2 electrode (charge voltage plateau = 4.3 V), illustrating excellent catalytic activity of Ru@PGE-2 catalysts toward OERs. The low charge potential of the

dx.doi.org/10.1021/nl500397y | Nano Lett. 2014, 14, 3145−3152

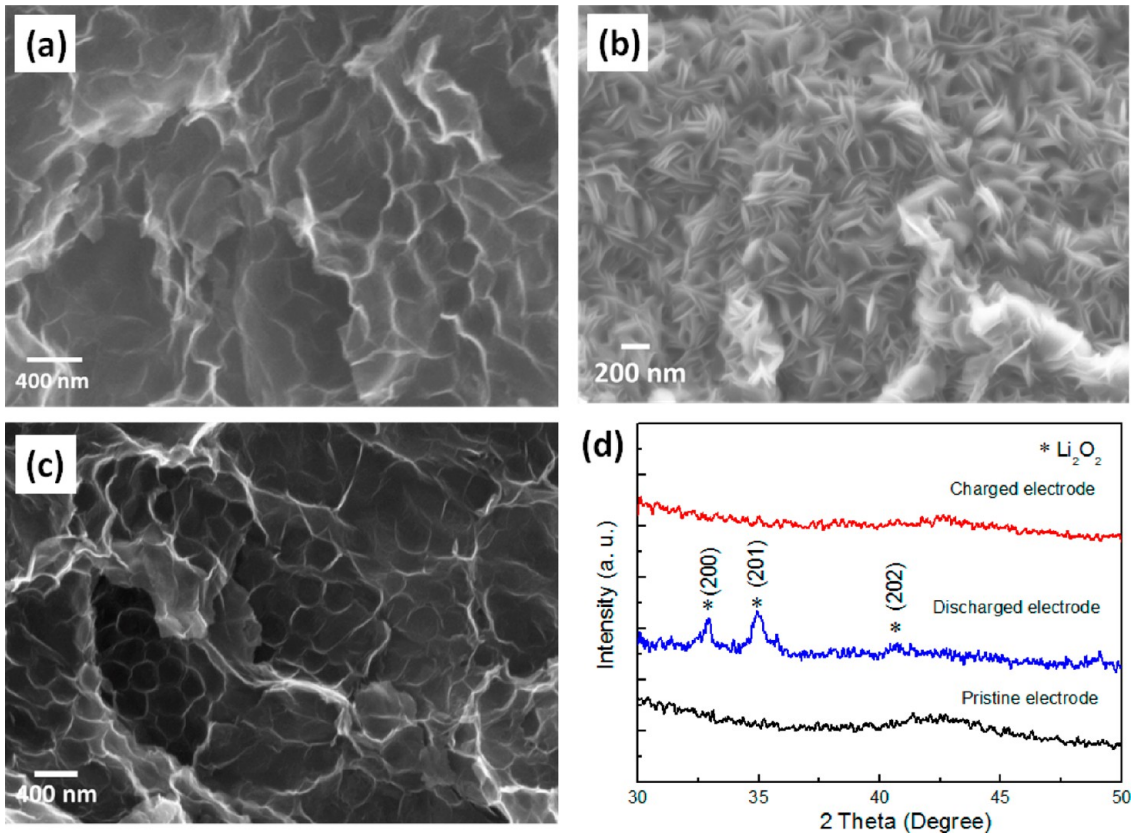

Figure 4. SEM observation of Ru@PGE-2 electrodes: (a) pristine electrode before cycling, (b) electrode discharged to 2.7 V at 200 mA g^{-1}, and (c) electrode recharged to 4.0 V at 200 mA g^{-1}. (d) XRD characterizations of Ru@PGE-2 electrodes before discharge after first discharge to 2.7 V and first recharge to 4.0 V at 200 mA g^{-1}.

Ru@PGE-2 catalyst is also consistent with our previously reported Ru@carbon black catalysts, which also demonstrated the high catalytic activity of Ru nanocrystals toward OERs in the Li−O_2 batteries.[36] Furthermore, it should be noted that 98.9% discharge capacity can be recharged below 4.0 V with a high energy efficiency of 86.8%. However, for the bare PGE-2 electrode most of the discharge capacity can only be recharged above 4 V with an energy efficiency of 72.5% in the voltage range of 2.0−4.4 V. The cycling performances of Ru@PGE-2 catalysts were first examined in the voltage range of 2.0−4.1 V at 500 mA g^{-1} (as shown in Figure S14e, Supporting Information). Even at an increased charge/discharge current density, the Ru@PGE-2 catalysts still achieved a low charge voltage plateau at about 3.2 V. Furthermore, the Ru@PGE-2 electrode demonstrated better capacity retention than the pristine porous graphene electrode in the first three cycles (Figure S14, Supporting Information).

The cycling performance of Ru@PGE-2 catalysts was further investigated by curtailing the capacity during cycling. Figure 3b shows the charge/discharge profiles of the Ru@PGE-2 electrode at 200 mA g^{-1} by curtailing the capacity to 500 mA h g^{-1}. There is no significant change of the charge/discharge curves and loss of specific capacity up to 200 cycles, indicating the good reversibility of the Ru@PGE-2 electrode. The charge voltage plateau of the Ru@PGE-2 electrode is about 3.6 V at 200 mA g^{-1} by curtailing the capacity to 500 mA h g^{-1}, which is higher than that of the Ru@PGE-2 electrode discharged to 2.0 V in the first cycle. The charge voltage differences may be due to the different Li_2O_2 decomposition mechanisms. Previous reports demonstrated that the decomposition of Li_2O_2 during charge process could undergo through two different pathways by using ab intio calculations and experimental investigations.[44,45]

$$Li_2O_2 \rightarrow Li^+ + e^- + LiO_2 \quad (1)$$

$$LiO_2 + LiO_2 \rightarrow Li_2O_2 + O_2 \quad (2)$$

Or

$$Li_2O_2 \rightarrow 2Li^+ + 2e^- + O_2 \quad (3)$$

The first pathway is associated with the delithiation of Li_2O_2 to form LiO_2-like species in the first step via a solid-solution route (eq 1). In the second step, the metastable LiO_2 disproportionates to evolve O_2, yielding an overall $2e^-/O_2$ oxygen evolution process (eq 2). The second pathway involves direct electrochemical decomposition of Li_2O_2 to form Li^+ and O_2 via a two-phase transition (eq 3). The charge overpotential of the decomposition of Li_2O_2 through the first pathway is lower than that through the second pathway.

The comparison of charge/discharge curves of Ru@PGE-2 catalysts in the first cycle with different capacity limitation is shown in Figure S16 (Supporting Information). It is observed that the charge voltage curves of Ru@PGE-2 electrode showed three stages. When the capacity is limited to 500 or 1000 mA h g^{-1}, the initial charge stage showed a sloping profile at low voltage (<3.6 V), corresponding to the Li_2O_2 decomposition through the first pathway. The second charge stage showed a voltage plateau at about 3.6 V, corresponding to the Li_2O_2 decomposition through the second pathway. The third charge stage is the voltage sloping higher than 3.6 V, corresponding to

dx.doi.org/10.1021/nl500397y | Nano Lett. 2014, 14, 3145−3152

the decomposition of byproducts and electrolyte. When increasing the charge/discharge capacity limitation, we observed that the initial low voltage slope extended to a plateau at about 3.1 V. This indicates that the ratio of Li_2O_2 decomposed though the first pathway increased.

The Ru@PGE-2 electrode also showed high energy efficiency of 78.9% in the first cycle, which still maintained at 77.8% at the 200th cycle (Figure 3c). When increasing the capacity limitation to 1000 mA h g^{-1}, the Ru@PGE-2 electrode shows excellent cycling stability up to 100 cycles with an average energy efficiency of 78.1% (Figure 3d,e). When the Li−O_2 batteries were cycled at a higher current density (500 mA g^{-1}), the Ru@PGE-2 electrode also showed very stable discharge performances with almost no change of the discharge curves for 200 cycles and only a small increase in the charge overpotential by curtailing the capacity to 1000 mA h g^{-1} (Figure S17, Supporting Information). The increase of the charge overpotential could be caused by the increased impedance of Li−O_2 cells upon cycling (as shown in Figure S18, Supporting Information). The dominant reactions of rechargeable Li−O_2 batteries are the formation and decomposition of Li_2O_2 during discharge/charge processes. However, there are also some byproducts formed during charge/discharge processes due to the reaction of carbon materials with electrolyte. Those byproducts, such as Li_2CO_3, cannot be totally decomposed during the charge process. The accumulation of byproducts upon cycling could induce the increase of the impedance of Li−O_2 cells. The energy efficiencies of the Li−O_2 batteries maintained at 70% after 200 cycles at such high charge/discharge current density (Figure S17d, Supporting Information). Extending the capacity limitation to 2500 mA h g^{-1}, the Ru@PGE-2 electrode can still show excellent cycling stability and high energy density (Figure S19, Supporting Information). The charge/discharge voltage profiles in the initial five cycles with various capacity limitations are presented in Figure S20 (Supporting Information). All Ru@PGE-2 electrodes show stable charge/discharge voltage profiles after the third cycle, indicating the good cycling stability. The high C-rate performances of Li−O_2 cells were further tested with the increased current densities from 200 to 2000 mA g^{-1} (as shown in Figure 3f). Although the current density has been raised 10-fold, the Li−O_2 battery still shows a good reversibility for the ORRs and OERs with the discharge voltage plateau at 2.6 V and the charge voltage plateau at 3.8 V at 2000 mA g^{-1}, confirming good high C-rate performance. The high C-rate performance and good reversibility could be ascribed to the porous architecture of the graphene electrode and highly efficient Ru nanocrystals, which allow efficient oxygen diffusion throughout the electrode and provide high catalytic activity toward ORRs and OERs.

The electrode morphologies of the Ru@PGE-2 electrodes were observed by FESEM (Figure 4). After discharging the cell to 2.7 V, the Ru@PGE-2 electrode was covered by the discharge products (Li_2O_2) as shown in Figure 4b. The morphology of Li_2O_2 consists of bundles of nanosheets. Some of them form into toroidal structures, which is consistent with the recent reports.[12,46] When charging the cell back to 4 V, all discharge products completely disappeared (Figure 4c), indicating high reversibility of the Ru@PGE-2 electrode. The discharge products of the Ru@PGE-2 electrodes were further analyzed by XRD as shown in Figure 4d. The dominant discharge products after the first cycle discharge to 2.7 V can be identified to be Li_2O_2. After recharge, all discharge products were removed from the electrode. Furthermore, we still observed the XRD peaks of Li_2O_2 after 100 cycles at 500 mA g^{-1} by curtailing the capacity to 1000 mA g^{-1} (Figure S21, Supporting Information). Previous studies report that carbon materials are unstable on charging above 3.5 V in the presence of dominant discharge product of Li_2O_2 in the DMSO based electrolyte.[47] The reaction between carbon materials with electrolyte and discharge products cannot be totally avoided. In order to investigate the stability of Ru@PGE-2 catalysts, Raman spectroscopy measurement was conducted on the electrodes before and after 100 cycles at 500 mA g^{-1} by curtailing the capacity to 1000 mA h g^{-1} (as shown in Figure S22, Supporting Information). The D band at about 1350 cm^{-1} is ascribed to edges, disordered carbon, and other defects, while, the G band at 1600 cm^{-1} corresponds to ordered sp^2 bonded carbon.[48,49] The I_D/I_G intensity ratio indicates the disorder degree and the average size of sp^2 domains. As shown in Table S1 (Supporting Information), I_D/I_G ratio only slightly increased after 100 cycles, which indicated that the porous graphene is relatively stable as the cathode catalyst for Li−O_2 batteries.

The above results demonstrate that Li−O_2 cells with appropriately designed cathode catalysts can operate reversibly with high specific capacity, high energy efficiency, and good cycling stability. The much improved electrochemical performance could be attributed to the high efficient Ru nanocrystal catalysts combined with porous graphene nanoarchitecture. The Ru nanocrystals can significantly reduce the charge overpotential. This effect not only increases the energy efficiency but also reduces the electrolyte decomposition at high charge voltages.[47] Furthermore, the porous graphene with large pore size can provide sufficient spaces to accommodate the discharge products, thus effectively reducing the volume change during the charge/discharge. Therefore, the Li−O_2 batteries with Ru@PGE-2 catalysts exhibit excellent stable cycling performance during charge/discharge.

Conclusions. In summary, we report the achievement of high-performance Li−O_2 batteries with Ru@porous graphene catalysts, which exhibited a high specific capacity of 17 710 mA h g^{-1} and a high energy efficiency of 86.8%. The porous graphene catalysts were investigated to reveal the relationship between porous structure and catalytic performances. Ru nanocrystals were further decorated on porous graphene matrix and demonstrated superior cycle stability at different current densities up to 200 cycles at a curtailing capacity of 1000 mA h g^{-1}. We also showed that Ru@PGE-2 catalysts can effectively decompose the discharge product Li_2O_2, facilitate the OERs, and lead to a high round-trip efficiency. Therefore, Ru-functionalized porous graphene is a promising cathode catalyst for rechargeable Li−O_2 batteries with low charge overpotential, long cycle life, and high specific capacity.

■ ASSOCIATED CONTENT

Supporting Information

Experimental section, SEM, BET, TGA, and XRD characterizations and electrochemical examination of prepared materials. This material is available free of charge via the Internet at http://pubs.acs.org.

■ AUTHOR INFORMATION

Corresponding Author

*E-mail: Guoxiu.Wang@uts.edu.au.

Notes

The authors declare no competing financial interest.

■ ACKNOWLEDGMENTS

This project was financially supported by the Australian Research Council (ARC) through the ARC FT project (FT110100800).

■ REFERENCES

(1) Abraham, K. M.; Jiang, Z. *J. Electrochem. Soc.* **1996**, *143*, 1−5.
(2) Lee, J. S.; Kim, S. T.; Cao, R.; Choi, N. S.; Liu, M.; Lee, K. T.; Cho, J. *Adv. Energy Mater.* **2011**, *1*, 34−50.
(3) Bruce, P. G.; Freunberger, S. A.; Hardwick, L. J.; Tarascon, J. M. *Nat. Mater.* **2012**, *11*, 19−29.
(4) Girishkumar, G.; McCloskey, B.; Luntz, A. C.; Swanson, S.; Wilcke, W. *J. Phys. Chem. Lett.* **2010**, *1*, 2193−2203.
(5) Christensen, J.; Albertus, P.; Sanchez-Carrera, R. S.; Lohmann, T.; Kozinsky, B.; Liedtke, R.; Ahmed, J.; Kojic, A. *J. Electrochem. Soc.* **2012**, *159*, R1−R30.
(6) Li, F. J.; Zhang, T.; Zhou, H. S. *Energy Environ. Sci.* **2013**, *6*, 1125−1141.
(7) Ogasawara, T.; Debart, A.; Holzapfel, M.; Novak, P.; Bruce, P. G. *J. Am. Chem. Soc.* **2006**, *128*, 1390−1393.
(8) Peng, Z. Q.; Freunberger, S. A.; Hardwick, L. J.; Chen, Y. H.; Giordani, V.; Barde, F.; Novak, P.; Graham, D.; Tarascon, J. M.; Bruce, P. G. *Angew. Chem., Int. Ed.* **2011**, *50*, 6351−6355.
(9) Peng, Z. Q.; Freunberger, S. A.; Chen, Y. H.; Bruce, P. G. *Science* **2012**, *337*, 563−566.
(10) Xiao, J.; Wang, D. H.; Xu, W.; Wang, D. Y.; Williford, R. E.; Liu, J.; Zhang, J. G. *J. Electrochem. Soc.* **2010**, *157*, A487−A492.
(11) Tran, C.; Yang, X. Q.; Qu, D. Y. *J. Power Sources* **2010**, *195*, 2057−2063.
(12) Mitchell, R. R.; Gallant, B. M.; Thompson, C. V.; Shao-Horn, Y. *Energy Environ. Sci.* **2011**, *4*, 2952−2958.
(13) Xiao, J.; Mei, D. H.; Li, X. L.; Xu, W.; Wang, D. Y.; Graff, G. L.; Bennett, W. D.; Nie, Z. M.; Saraf, L. V.; Aksay, I. A.; Liu, J.; Zhang, J. G. *Nano Lett.* **2011**, *11*, 5071−5078.
(14) Sun, B.; Liu, H.; Munroe, P.; Ahn, H.; Wang, G. X. *Nano Res.* **2012**, *5*, 460−469.
(15) Wang, Z. L.; Xu, D.; Xu, J. J.; Zhang, L. L.; Zhang, X. B. *Adv. Funct. Mater.* **2012**, *22*, 3699−3705.
(16) Xu, J. J.; Wang, Z. L.; Xu, D.; Zhang, L. L.; Zhang, X. B. *Nat. Commun.* **2013**, *4*, 3438.
(17) Guo, Z.; Zhou, D.; Dong, X.; Qiu, Z.; Wang, Y.; Xia, Y. *Adv. Mater.* **2013**, *25*, 5668−5672.
(18) Sun, B.; Wang, B.; Su, D. W.; Xiao, L. D.; Ahn, H.; Wang, G. X. *Carbon* **2012**, *50*, 727−733.
(19) Li, Y. L.; Wang, J. J.; Li, X. F.; Geng, D. S.; Li, R. Y.; Sun, X. L. *Chem. Commun.* **2011**, *47*, 9438−9440.
(20) Shao, Y. Y.; Park, S.; Xiao, J.; Zhang, J. G.; Wang, Y.; Liu, J. *ACS Catal.* **2012**, *2*, 844−857.
(21) Li, Y. L.; Wang, J. J.; Li, X. F.; Liu, J.; Geng, D. S.; Yang, J. L.; Li, R. Y.; Sun, X. L. *Electrochem. Commun.* **2011**, *13*, 668−672.
(22) Li, Y. L.; Wang, J. J.; Li, X. F.; Geng, D. S.; Banis, M. N.; Li, R. Y.; Sun, X. L. *Electrochem. Commun.* **2012**, *18*, 12−15.
(23) Nie, H.; Zhang, H.; Zhang, Y.; Liu, T.; Li, J.; Lai, Q. *Nanoscale* **2013**, *5*, 8484−8487.
(24) Debart, A.; Bao, J.; Armstrong, G.; Bruce, P. G. *J. Power Sources* **2007**, *174*, 1177−1182.
(25) Debart, A.; Paterson, A. J.; Bao, J.; Bruce, P. G. *Angew. Chem., Int. Ed.* **2008**, *47*, 4521−4524.
(26) Oh, S. H.; Nazar, L. F. *Adv. Energy Mater.* **2012**, *2*, 903−910.
(27) Black, R.; Lee, J. H.; Adams, B.; Mims, C. A.; Nazar, L. F. *Angew. Chem., Int. Ed.* **2013**, *52*, 392−396.
(28) Xu, J. J.; Xu, D.; Wang, Z. L.; Wang, H. G.; Zhang, L. L.; Zhang, X. B. *Angew. Chem., Int. Ed.* **2013**, *52*, 3887−3890.
(29) Oh, S. H.; Black, R.; Pomerantseva, E.; Lee, J. H.; Nazar, L. F. *Nat. Chem.* **2012**, *4*, 1004−1010.
(30) Wang, H. L.; Yang, Y.; Liang, Y. Y.; Zheng, G. Y.; Li, Y. G.; Cui, Y.; Dai, H. J. *Energy Environ. Sci.* **2012**, *5*, 7931−7935.
(31) Li, F. J.; Ohnishi, R.; Yamada, Y.; Kubota, J.; Domen, K.; Yamada, A.; Zhou, H. S. *Chem. Commun.* **2013**, *49*, 1175−1177.
(32) Lu, Y. C.; Xu, Z. C.; Gasteiger, H. A.; Chen, S.; Hamad-Schifferli, K.; Shao-Horn, Y. *J. Am. Chem. Soc.* **2010**, *132*, 12170−12171.
(33) Lu, Y. C.; Gasteiger, H. A.; Shao-Horn, Y. *J. Am. Chem. Soc.* **2011**, *133*, 19048−19051.
(34) Harding, J. R.; Lu, Y. C.; Tsukada, Y.; Shao-Horn, Y. *Phys. Chem. Chem. Phys.* **2012**, *14*, 10540−10546.
(35) Jung, H. G.; Jeong, Y. S.; Park, J. B.; Sun, Y. K.; Scrosati, B.; Lee, Y. J. *ACS Nano* **2013**, *7*, 3532−3539.
(36) Sun, B.; Munroe, P.; Wang, G. X. *Sci. Rep.* **2013**, *3*, 2247.
(37) Li, F.; Tang, D.-M.; Chen, Y.; Golberg, D.; Kitaura, H.; Zhang, T.; Yamada, A.; Zhou, H. *Nano Lett.* **2013**, *13*, 4702−4707.
(38) Yilmaz, E.; Yogi, C.; Yamanaka, K.; Ohta, T.; Byon, H. R. *Nano Lett.* **2013**, *13*, 4679−4684.
(39) Jian, Z.; Liu, P.; Li, F.; He, P.; Guo, X.; Chen, M.; Zhou, H. *Angew. Chem., Int. Ed.* **2013**, *53*, 442−446.
(40) Huang, X. D.; Qian, K.; Yang, J.; Zhang, J.; Li, L.; Yu, C. Z.; Zhao, D. Y. *Adv. Mater.* **2012**, *24*, 4419−4423.
(41) Xu, D.; Wang, Z. L.; Xu, J. J.; Zhang, L. L.; Zhang, X. B. *Chem. Commun.* **2012**, *48*, 6948−6950.
(42) Trahan, M. J.; Mukerjee, S.; Plichta, E. J.; Hendrickson, M. A.; Abraham, K. M. *J. Electrochem. Soc.* **2013**, *160*, A259−A267.
(43) Jung, H. G.; Hassoun, J.; Park, J. B.; Sun, Y. K.; Scrosati, B. *Nat. Chem.* **2012**, *4*, 579−585.
(44) Lu, Y.-C.; Shao-Horn, Y. *J. Phys. Chem. Lett.* **2013**, *4*, 93−99.
(45) Kang, S.; Mo, Y.; Ong, S. P.; Ceder, G. *Chem. Mater.* **2013**, *25*, 3328−3336.
(46) Ottakam Thotiyl, M. M.; Freunberger, S. A.; Peng, Z.; Chen, Y.; Liu, Z.; Bruce, P. G. *Nat. Mater.* **2013**, *12*, 1050−1056.
(47) Thotiyl, M. M. O.; Freunberger, S. A.; Peng, Z. Q.; Bruce, P. G. *J. Am. Chem. Soc.* **2013**, *135*, 494−500.
(48) Stankovich, S.; Dikin, D. A.; Piner, R. D.; Kohlhaas, K. A.; Kleinhammes, A.; Jia, Y.; Wu, Y.; Nguyen, S. T.; Ruoff, R. S. *Carbon* **2007**, *45*, 1558−1565.
(49) Jung, I.; Dikin, D. A.; Piner, R. D.; Ruoff, R. S. *Nano Lett.* **2008**, *8*, 4283−4287.